3D Numerical Simulation of a Hovering Hummingbird-inspired Flapping Wing with Dynamic Morphing

Y. Dong†, B. Song, D. Xue and W. Yang

School of Aeronautics, Northwestern Polytechnical University, Xi'an 710072, PR China

†*Corresponding Author Emailxgddyb@mail.nwpu.edu.cn*

ABSTRACT

Three-dimensional numerical simulations are performed to examine the effects of dynamic wing morphing of a hummingbird-inspired flexible flapping wing on its aerodynamic performance in hovering flight. The range analysis and variation analysis in the orthogonal experiment are conducted to assess the significance level of various deformations observed in the hummingbird wings on wing aerodynamic performance. It has been found that both camber and twist significantly can affect lift, and twist has an even higher significant impact on lift efficiency. Spanwise bending, whether out-of-stroke-plane or in-stroke-plane, has a negligible impact on lift and efficiency, and the in-stroke-plane bending can cause lift to decrease to an extent. Optimal parameters for determining the wing deformations are selected and tested to validate the conclusions drawn in the analysis for the results in orthogonal experiment. Through a comparison study between the optimized wings and the rigid wing, it is found that although the wing flexibility can cause the net force to decrease, the flexible wing used less energy to bring the net force closer to the vertical direction, thereby improving the lift efficiency. This study provides an aerodynamics understanding of the efficiency improvement of the hummingbird-inspired flexible flapping wing.

NOMENCLATURE

A	area vector	p_n	static pressure
C_D	drag coefficient	R	semimajor axis
$\overline{C_D}$	time-averaged drag coefficient	Re	Reynolds number
C_F	net force	R_2	radius of second moment of area
C_L	lift coefficient	R_v	range
$\overline{C_L}$	time-averaged lift coefficient	r	any radial position
C_P	power coefficient	$\bar{r}$	normalized radial position
$\overline{C_P}$	time-averaged power coefficient	S	area of plane
C_ζ	control parameter of pitching angle waveform	SS	sum of squares of deviations
		T	period
c	semi-minor axis	Tr	successive rotation matrix
c_R	wing root chord	$t_1; t_2; t_3$	column vector
$\bar{c}$	mean chord	t	time instant
$c(\bar{r})$	local chord at any normalized radial position	U	average wingtip speed
		V	velocity vector
D	drag	$x; y; z$	coordinate axis
DF	degree of freedom	$x(\bar{r})$	local chordwise position at a given normalized radial position
df	degree of freedom of the ith factor		
F	F statistic	$\bar{x}(\bar{r})$	normalized local chordwise position at a given normalized radial position
F_X	horizontal force		
F_Z	vertical force	Y	sample average
f	frequency	y_n	test result of the nth sample
$h(\bar{r}, \bar{x}, t)$	cross-section height function	α_F	vector angle of net force
$h_m(\bar{r}, t)$	maximum cross-section height at a given normalized radial position	ζ	pitching angle
		$\zeta_{m,tip}$	amplitude in pitching angle at the tip
$h_m(r, t)$	maximum cross-section height	$\zeta_{m,root}$	amplitude in pitching angle at the root

	at a given radial position	$\zeta_m(r)$	amplitude in pitching angle at any radial position
$h_{m0,tip}$	amplitude in maximum cross-section height at the tip	η	lift efficiency
$h_{m0,root}$	amplitude in maximum cross-section height at the tip	υ	kinematic viscosity
$i; j; n$	index	ρ	density
K_i	sum of test results at ith level of a factor	$\boldsymbol{\tau}$	shear stress vector
k_i	average effect of a factor at ith level	Φ	flapping angle
L	lift	$\Phi_{m,root}$	amplitude in flapping angle at the root
l	distance traveled by a point at the wingtip per flapping cycle	$\Phi_{m,tip}$	amplitude in flapping angle at the tip
MS	mean deviation	$\Phi_m(r)$	amplitude in flapping angle at any radial position
MS_e	mean deviation corresponding to error	Φ_ζ	phase offset of the pitching angle relative to the flapping angle
N	constant	Ψ	elevation angle
Nm	number of samples in the orthogonal Experiment	$\Psi_{m,tip}$	amplitude in elevation angle at the tip
$Oxyz$	global coordinate system	$\Psi_{m,root}$	amplitude in elevation angle at the root
P	aerodynamic power	$\Psi_m(r)$	amplitude in elevation angle at any radial position
p	control parameter of chordwise camber	ω	spanwise vorticity
		$\overline{\omega}$	normalized spanwise vorticity

1. INTRODUCTION

Hummingbird-inspired flapping wing has attracted widespread attention because of its successful application in micro air vehicle (MAV) over the past decade. The Nano Hummingbird (Keennon *et al.* 2012), the robotic hummingbird (Coleman *et al.* 2015), and the ASL robot (Nan *et al.* 2017) are the most representative hummingbird-inspired flapping wing micro air vehicles (FW-MAVs). Phan and Park (2019) reviewed the design, fabrication, and testing of some bionic flapping wing robots. However, some of them could not fly freely using the control equipment and power onboard. In order to achieve high performance, FW-MAV need both a high aerodynamic force and high efficiency, which allow it to adjust the flight strategies to meet requirements for flexible maneuverability and long cruise duration in various applications. Aerodynamics and aeroelasticity represent the tough challenges faced by scientists and engineers in optimal design (Shyy *et al.* 2010).

Nowadays, hummingbird-inspired FW-MAVs exploit the unsteady aerodynamic mechanisms found in insect flight to enhance flight performances. Some researchers (Chin and Lentink 2016; Sane 2003) described those mechanisms in detail, including the stable attached leading-edge vortex (LEV), added mass, wake capture, rotational circulation, and clap-and-fling effects. Each mechanism is directly related to a specific wing motion. However, the anatomical differences between hummingbird wing and insect wing mean that hummingbird doesn't use the identical aerodynamic mechanisms as insect (Tobalske *et al.* 2007). So there have been plenty of studies on aerodynamic mechanisms in the flight of hummingbird so that the findings can become instructive for designing artificial flapping wing. In earlier studies (Wolf *et al.* 2013; Altshuler *et al.* 2009), Particle image velocimetry (PIV) experiments were adopted to characterize the

evolution of vortices in the flow field. Three-dimensional high-frequency vision measurement technology has been introduced to capture vital features of hummingbird flight recently (Masateru *et al.* 2017). Technologies like those make it feasible to combine the unsteady aerodynamic theory, computational fluid dynamics (CFD), and experimental measurement to accurately predict aerodynamic forces and power consumption during hummingbird flight. In spite of the fact that hummingbirds of different species may have distinct wakes in hovering flight, researchers (Yang and Zhang 2015; Song *et al.* 2014) have agreed that LEV plays a crucial role in the flight of hovering hummingbird. Even so, hummingbird aerodynamics remains not fully understood due to the highly complex morphology of vertebrate wings. Similarly, it is not simple for a designer to make an artificial flapping wing that mimics the mechanical behavior of hummingbird wings and follows an identical motion (Reid *et al.* 2021). Besides, there exist generally multiple primary factors involved in the effects on aerodynamic performance. The influence of a single variable is difficult to assess because of the interplay of various factors. As a result, the study on the aerodynamics of hummingbird flight can only provide limited help for designing the artificial hummingbird-inspired flapping wing.

For hummingbird with vertebrate wings, it can use muscles and skeletal joints to modulate the aerodynamic and inertial forces required for aerial maneuvers and perturbation recovery. Masateru *et al.* (2017) reconstructed the right wing of a hummingbird from the profile and the feather shafts. The time-varying wing deformations, such as spanwise in-stroke-plane bending, out-of-stroke-plan bending, twist, and the camber in cross sections, were quantified, and the possible causes of those remarkable dynamic deformations were briefly analyzed. Nowadays, almost all hummingbird-inspired flapping wings made with light and soft materials have the feature of passive

elastic deformations. Some of them have been able to achieve positive camber and linear twists during the flapping flight. Such new intelligent actuators as artificial muscle, shape memory alloy, piezoelectric and electromagnetic actuators have great potential applications on wing shape active control for the future bionic flapping systems, and the availability of the wings with autonomic deformability will revolutionize the development of FW-MAVs. Therefore, it is of practical significance to figure out how dynamic wing morphing affect wing performance.

The efficiency of flapping wing depends strongly on the kinematics and morphology of wing. Wing twist can compensate for the spanwise increase in the geometric angle of attack because of flapping during flight and cause a decrease in only the required aerodynamic power (Walker *et al.* 2009). Camber can improve flow attachment to the wing, enhance lift by accelerating more of the flow at the suction side of the wing, and delay flow separation (Shyy *et al.* 2016). A combination of camber and twist had similar results to a single influence of camber. That increased lift by 10%, reduced the aerodynamic power consumption by 5% and increased the overall efficiency by 17% (Noyon *et al.* 2014). However, the above studies focus on the effects of the chordwise deformations at low Reynold numbers (~10^2). And the aerodynamic performance is dominated by the flow field around the insect-like flapping wings. Therefore, extra effort is required to analyze their effects at relatively higher Reynolds numbers (10^3~10^4). Roccia *et al.* (2017) numerically studied the effect of spanwise bending on lift generation in flapping wings, and their results implied that the in-plane bending affected the lift force in specific zones of the stroke cycle, and the out-of-plane bending affected the lift throughout the stroke cycle. Flexible flapping wings can form spanwise and chordwise deformations and reduce inertial forces harmful to their aerodynamic performance during the high-frequency flapping (Phan *et al.* 2016b). As a result, more and more researchers (Bhattacharjee *et al.* 2019; Phan *et al.* 2016b, 2017; Gehrke *et al.* 2021, 2018) are paying attention to aerodynamic optimization to minimize the energy cost of hovering flight. Various theoretical models (Xuan *et al.* 2020) were adopted to estimate the performance of twist wings without expensive computational cost expended. To our knowledge, for hummingbird-inspired flapping wing at a higher Reynolds number, the effect of wing flexibility on aerodynamic performance has not been studied.

In the present work, we built a hummingbird-inspired wing model, in which the various deformations mentioned above were all incorporated to evaluate the key parameters for determining wing aerodynamic performance in hover. The deformations were prescribed directly in a more controlled way, which allowed us to investigate their effects by solving the Navier-Strokes equations without considering complex fluid and structure interaction modeling. Numerical simulations were planned through orthogonal design, from which the locally optimal solutions were available. A comparative study for the optimized wings and the rigid wing was performed to evaluate the gain due to wing flexibility. We also explored further and discussed the reasons behind the differences in aerodynamic performance from the perspective of the flow field visualization and net forces. The results can provide helpful instruction for the design in FW-MAVs and lay the foundation for future optimization research.

2. MODEL AND METHOD

2.1 Wing model

The model has a quarter-elliptical plane (Fig. 1) with semimajor and semi-minor axes of $R = 70mm$ and $c = 24.8mm$, respectively. No offset is present between the root and the center of the flapping axis. As a result, the wing has a mean chord $\overline{c} = 19.5mm$, an area of plane $S = 0.00136m^2$, and a radius of second moment of area $R_2 = \sqrt{1/S \int_0^R r^2 c(r) = dr} = 35mm$, where $c(r)$ is the chord at any radial position r. In addition, the model thickness is $0.4mm$ ($2\%c$), and it is so thin that the thickness effect is negligible. This wing resembles the right wing of a realistic hummingbird (Tanaka *et al.* 2013) in terms of morphology. The
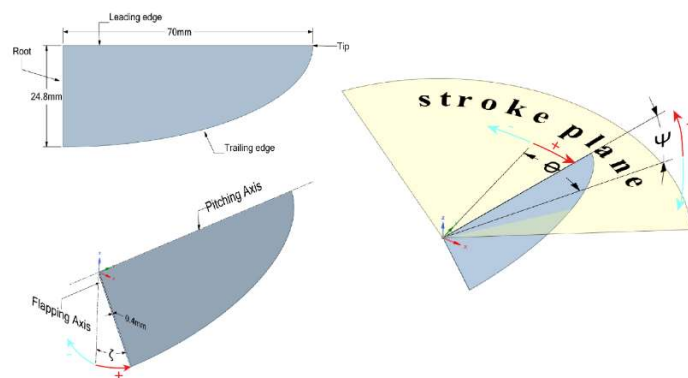

Fig. 1. Schematic of the wing geometry, the global coordinate system, and the angle definitions of wing motion.

air used for numerical simulations has a density ρ of $1.205 kg/m^{-3}$ and a kinematic viscosity $\nu = 15.02 mm^2/s$. We imposed a flapping frequency $f = 28.7 Hz$ to yield the Reynolds number (Re), and the definition of $Re = U\bar{c}/\nu$ with $U = fl$, in which l is the distance traveled by a point at the wingtip per flapping cycle, was adopted here. Three-dimensional numerical simulations were performed at a relatively higher Reynolds number ($Re = 10^4$), which is within the Reynolds number of the hummingbird hovering flight (Nan *et al.* 2017). The maximum cross-section amplitude in flapping angle was confined to **55°**, so wings in current studies were guaranteed to have a same Reynolds number.

2.2 Wing kinematics and dynamic morphing

$Oxyz$ is a fixed global coordinate system (see Fig. 1), where the origin is at the wing base, x and y form the horizontal plane (x points backward), and the z-direction is vertical. The stroke plane angle is the angle between the stroke plane and the horizontal plane. There exists usually a slight stroke plane angle of about 12.5° observed in hovering hummingbirds. But given no incoming flow speed in quiescent air, we confined the stroke plane to a horizontal plane, ignoring the effect of the stroke plane angle.

Here a rigid wing model was presented to illustrate the three Euler angles at a cross section. As shown in Fig. 1, the flapping angle Φ and the elevation angle Ψ describe the in-stroke-plane and the out-of-stroke-plane motions, respectively. The flapping angle is the angle between the y-axis and the projection of the leading edge to the stroke plane. The elevation angle is the dihedral angle between the stroke plane and the leading edge. The pitching angle is the rotation angle around the pitching axis, which is the leading edge of the middle wing surface. The schematic has marked the positive directions of the three angles with the arrows. Both the flapping angle and the elevation angle are defined in the inertial system, while the pitching angle is the rotation angle around the moving axis that rotates back and forth around the z-axis in the global coordinate system. We write the successive rotation matrix to specify the coordinate transformation of a point on the wing as

$$Tr = [t_1 \quad t_2 \quad t_3],$$

$$t_1 = \begin{bmatrix} \cos\Phi\cos\zeta - \sin\Phi\sin\Psi\sin\zeta \\ -\sin\Phi\cos\zeta - \cos\Phi\sin\Psi\sin\zeta \\ \cos\Psi\sin\zeta \end{bmatrix},$$

$$t_2 = \begin{bmatrix} \cos\Psi\sin\Phi \\ \cos\Phi\cos\Psi \\ \sin\Psi \end{bmatrix},$$

$$t_3 = \begin{bmatrix} -\cos\Phi\sin\zeta - \sin\Phi\sin\Psi\cos\zeta \\ \sin\Phi\sin\zeta - \cos\Phi\sin\Psi\cos\zeta \\ \cos\Psi\cos\zeta \end{bmatrix}. \quad (1)$$

Multiplying the initial coordinate of each node by the transformation matrix will give the three-dimensional coordinate at any time instant. The camber in cross sections, defined as the ratio of the

maximum cross-section height to the chord, will be specified as a positive value if the chord arches upward in the direction perpendicular to the wing surface.

Several approximations and assumptions were made to simplify the modeling. The spanwise distribution of each angle was assumed to be linear and independent of time. The time courses of normalized angles were identical across all sections. We multiplied the shape function (the spatial distribution of an angle) by the normalized time courses to determine the variation of an angle in time and space. Those distributions have been found to be approximately linear in the hovering FW-MAV, so it made sense to do this. To model the hummingbird-inspired flapping wing, we attempted to extract as many features from the hovering hummingbird as possible instead of replicating the actual flapping completely, which allowed us to distinguish effect of each deformation.

The flapping angle $\Phi(r,t)$ at any radial position is described by a cosinoidal oscillation,

$$\Phi_m(r) = \Phi_{m,root} + (\Phi_{m,tip} - \Phi_{m,root})r/R,$$
$$\Phi_m(r,t) = \Phi_m(r)\cos(2\pi ft), \quad (2)$$

where $\Phi_{m,root}$, $\Phi_{m,tip}$, and $\Phi_m(r)$ are the amplitudes of the flapping angles at the root, the tip and any radial position, respectively, and t is a given time instant. Note that the other two angles follow the same naming rules. The functional form was inspired by the flapping motions of the robotic wing experiments. The elevation angle $\Psi(r,t)$, appears as a sinusoidal oscillation,

$$\Psi_m(r) = \Psi_{m,root} + (\Psi_{m,tip} - \Psi_{m,root})r/R,$$
$$\Psi_m(r,t) = \Psi_m(r)\sin(2\pi Nft), \quad (3)$$

where N is either 1 or 2: $N = 1$ corresponds to one vertical oscillation per stroke period, and $N = 2$ corresponds to a figure-of-8 motion. The elevation angle is absent in most insect-like robotic wing experiments, but the elliptical wingtip trajectory can describe the hovering flight of hummingbird more realistically. Next, the pitching angle $\zeta(r,t)$ is described by a periodic hyperbolic function,

$$\zeta_m(r) = \zeta_{m,root} + \frac{(\zeta_{m,tip} - \zeta_{m,root})r}{R},$$
$$\zeta_m(r,t) = -\frac{\zeta_m(r)}{\tanh C_\zeta}\tanh[C_\zeta\sin(2\pi Nft + \Phi_\zeta), \quad (4)$$

where Φ_ζ is the phase offset of the pitching angle relative to the flapping angle, and C_ζ is a parameter that controls the waveform and determines the rotation duration during the stroke transition.

In the present study, only the symmetry of the wing rotation was considered, which caused the pitching angle phase offset to have a value of 0. As C_ζ approaches 0, $\zeta(r,t)$ becomes sinusoidal, and as $C_\zeta \to 0$, $\zeta(r,t)$ tends toward a step function (see Fig. 2). The upper bound of $C_\zeta = 5$ was adopted in a study on bionic kinematics by Kim and Han (2014), so we also set this value to 5. The time course of the non-dimensional pitching angle was
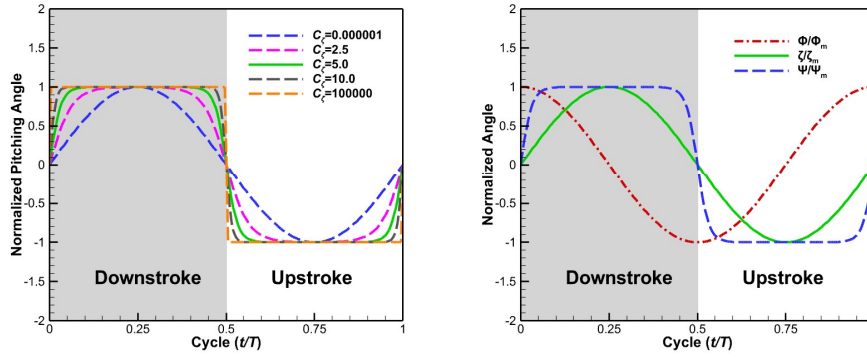
Fig. 2. Normalized pitching angle changed with C_ζ, and the profiles of the normalized flapping angle, elevation angle, and pitching angle during a stroke period in the present study.
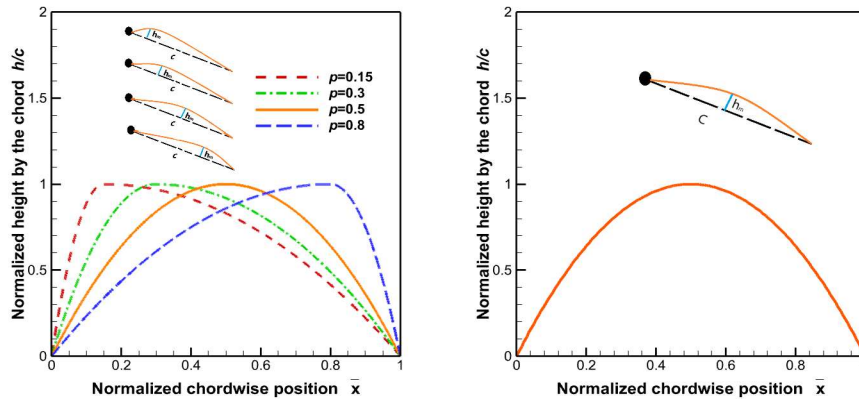

Fig. 3. Mean lines of NACA four-digit wing sections that are regulated by the different values of p, and the case corresponding to $p = 0.5$.

plotted in Fig. 2, along with the profiles of the non-dimensional flapping angle and elevation angle.

For the camber in cross sections as seen in Fig. 3, we used the equation of the mean lines of NACA four-digit wing sections:

$$\overline{r} = r/R,$$
$$c(\overline{r}) = c\sqrt{1-\overline{r}^2},$$
$$\overline{x}(\overline{r}) = x(\overline{r})/c(\overline{r}),$$
$$h(\overline{r},\overline{x},t) =$$
$$\begin{cases} \quad\quad (0 \le \overline{x} \le p) \\ h_m(\overline{r},t)/p^2(2p\overline{x} - \overline{x}^2) \\ \quad\quad (p < \overline{x} \le 1) \\ h_m(\overline{r},t)/(1-p^2)[(1-2p) + 2p\overline{x} - \overline{x}^2] \end{cases}, \quad (5)$$

where $x(r)$ is the chordwise position, $\overline{x}(\overline{r})$ is its normalized value by the local chord $c(\overline{r})$, $h_m(\overline{r},t)$ is the maximum cross-section height relative to the undeformed flat wing at the given radial position $\overline{r}$, p is the normalized chordwise position where the maximum wing height occurs, and $h(\overline{r},\overline{x},t)$ is the cross-section height at the given position $(\overline{r},\overline{x})$. We assumed that the maximum height of the mean line was in the mid-chord, i.e. p = 0.5, and thus the camber $h(\overline{r},\overline{x},t)/c(\overline{r})$ was determined by $h_m(\overline{r},t)$. The camber and pitching angle were believed to follow a similar profile that was expressed as follows:

$$h_m(\overline{r}) = h_{m0,root} + (h_{m0,tip} - h_{m0,root})\overline{r},$$

$$h_m(r,t) = \frac{h_{m0}(\overline{r})}{\tanh C_\zeta}\tanh[\,C_\zeta \sin(2\pi Nft + \Phi_\zeta)], \quad (6)$$

where $h_{m0,root}$, $h_{m0,tip}$ and $h_{m0}(\overline{r})$ are the maximum height at the root, the tip and any normalized radial position, respectively. The camber and twist have a strong coupling interaction, and similar treatments were found in another study by Du and Sun (2008).

In Eqs. (1) - (6), there are a total of 13 parameters for defining a stroke cycle. The frequency, the amplitude of the flapping angle at the tip, the elliptical wingtip trajectory, the control parameter of the pitching angle waveform, the pitching phase offset, and the normalized chordwise position where the maximum camber occurs have been determinate previously. Generally speaking, there should be no elevation angle at the root ($\Psi_{m,root} = 0$) because the intersection of the root and the leading edge is the origin of the reference system for the motion description, and there should be no camber ($h_{m0,tip} = 0$) at the wingtip due to the lack of the chord. Considering that hummingbird wings are at a high attack of angle during the hovering flight, we set the amplitude of the pitching angle at the root at 25° ($\zeta_{m,root} = 25°$). Wing morphing can be adjusted by changing the remaining four parameters (see Table 2).

2.3 Computational fluid dynamics

2.3.1 Computational domain and boundary

In Fig. 4, we depicted the wing planform as a three-dimensional membrane. The pivot point is the intersection of the leading edge and the root. The numerical model was built for only the right wing. As shown in Fig. 5, a half-cylinder with a radius and height of 12R was used as the computational domain. The wing is located 6R below the inlet. The symmetrical plane was imposed parallel to the *zx* plane. The flapping axis and symmetric plane are 20*mm* apart, a distance sufficient to eliminate clap-and-fling effect (Phan *et al.* 2016a). A mesh consists of two parts, the background mesh representing the wind tunnel and a separate component mesh covering the wing. Fluent allows us to build up the computation domain from overlapping meshes—also known as overset methodology. The case was created by specifying

the outer boundary of the foreground mesh as overset (boundary type) and creating an overset interface containing the two cell zones. In addition, at the inlet, outlet, and far field, the velocity was set to be 0.

2.3.2 Grid and solver

The grid was generated by the commercial meshing software ANSYS Meshing, and it is the finest around the wing and becomes coarser toward the far-field region (see Fig. 6). The wing surface was meshed into triangles with element edge lengths of about 0.4mm (Fig. 4). A high-density region with a radius of 2R was built around the wing. Inside that, the minimum edge length is 0.4*mm* at the cell layer around the walls, and the maximum is 24*mm* toward the boundary. The tetra growth rate away from the high-density region is 1.1. But the maximum edge length is 36*mm*, and the tetra growth rate is 1.2 outside of that area.
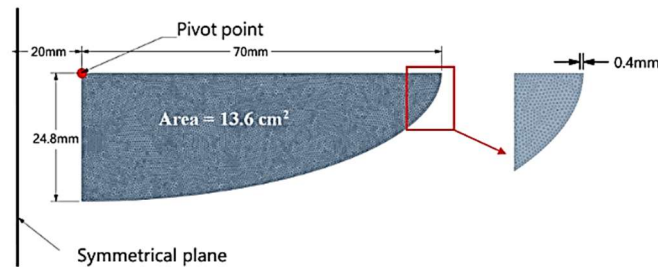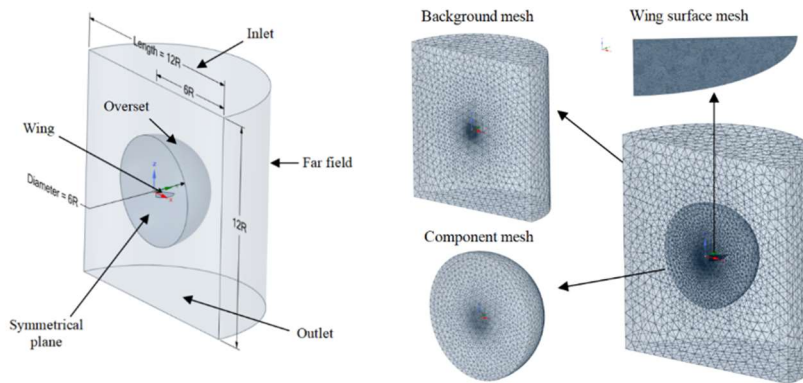

Fig. 4. Planform and the surface mesh of the wing.

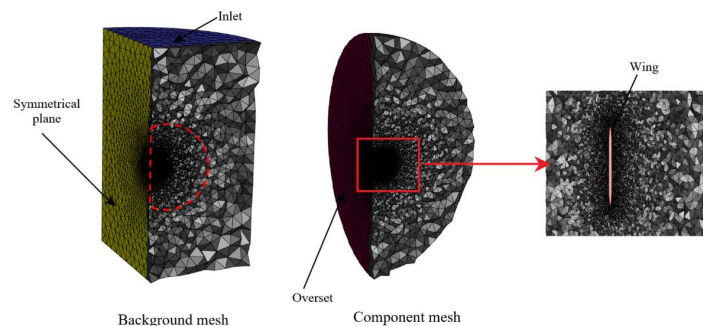**Fig. 5. Computational domain, overset component and background mesh.**

Fig. 6. Cross section of the computational domain.

Table 1 Sizes of three tested grids.

Grid	s_1 (mm)	s_2 (mm)	s_3 (mm)	No. cells of the component mesh	No. cells of the background mesh	Total no. cells (million)
1	0.57	34	51	883,449	131,633	~1.02
2	0.40	24	36	1,476,569	221,584	~1.70
3	0.28	17	25	2,695,709	426,609	~3.12

Table 2 Choice of factors and levels in the orthogonal experiments.

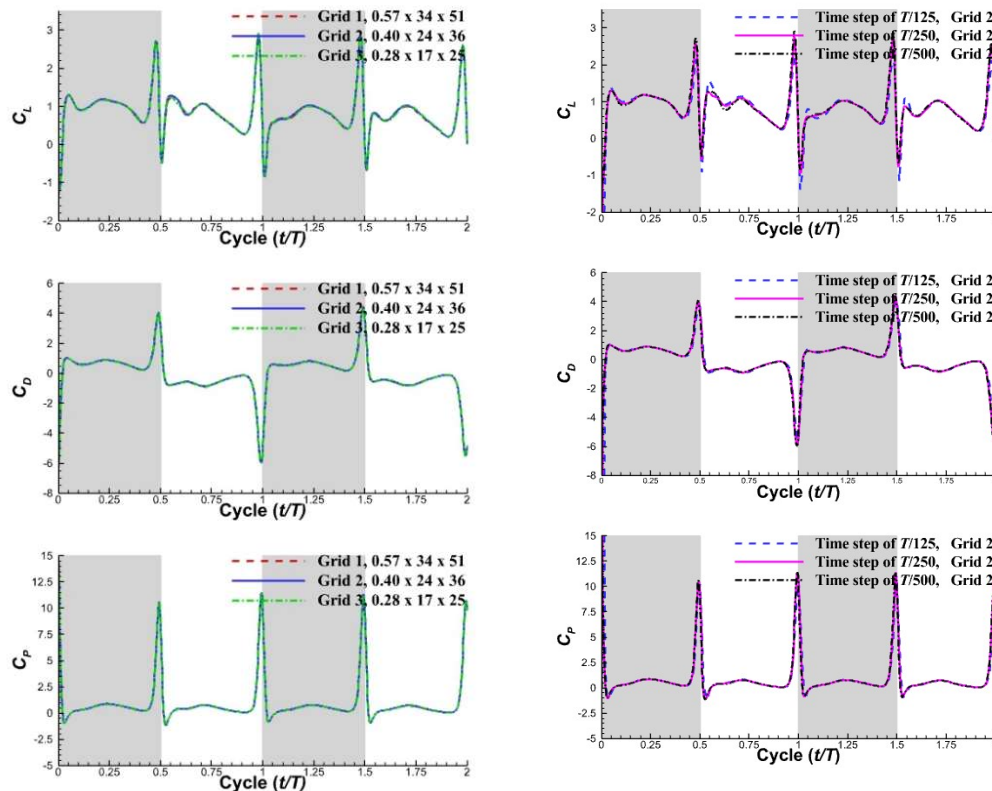| Factor / Level	$\Phi_{m,root}$	$\Psi_{m,tip}$	$\zeta_{m,tip}$	$h_{m0,root}$ (c_R)
1	47.5°	2.5°	37.5°	4%
2	50.0°	5.0°	50.0°	8%
3	52.5°	7.5°	62.5°	12%
4	55.0°	10.0°	75.0°	16%

Fig. 7. Lift, drag and aerodynamic power coefficients using three grids.

We computed the flow using the commercial software ANSYS Fluent and simulated the wing motion using the dynamic mesh feature with a user-defined function. A macro—DEFINE-GRIND-MOTIO—was applied to update the positions of the nodes on the wing mesh. The tetrahedral cells were deformed or reconnected to a new overset interface at each time step to adapt to changes in the position of the wing. The flow surrounding the flapping wing in hover was assumed to be laminar without considering the effect of turbulence in this realm. Similar CFD with the laminar model was explored in previous studies. Second-order discretization in time and space was implemented, and the coupled algorithm was used to solve the problem.

2.3.3 Independence of grids and time steps

The number of cells in a grid depends on three parameters: the maximum cell edge length on the wing surface, denoted by s_1, the maximum cell edge length in the high-density region, denoted by s_2, and the maximum cell edge on the boundary of the background mesh, denoted by s_3. Three girds were considered, and Table 1 displays their values. The results calculated for a case in the first two cycles using the three grids were plotted in Fig. 7. In this case, $\Phi_{m,root} = 47.5°$, $\zeta_{m,tip} = 62.5°$, $\Psi_{m,tip} = 7.5°$ and $h_{m0,root} = 12\%c$. And the motion of the wing during a stroke period was shown in Fig. 8. We defined the wing lift (L) as the
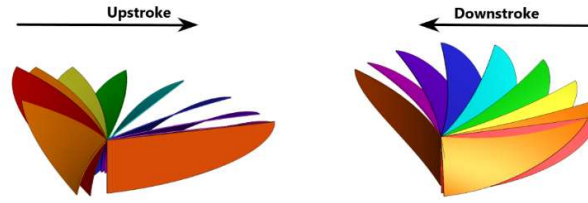
Fig. 8. Kinematics and dynamic morphing of the right wing during a stroke period.
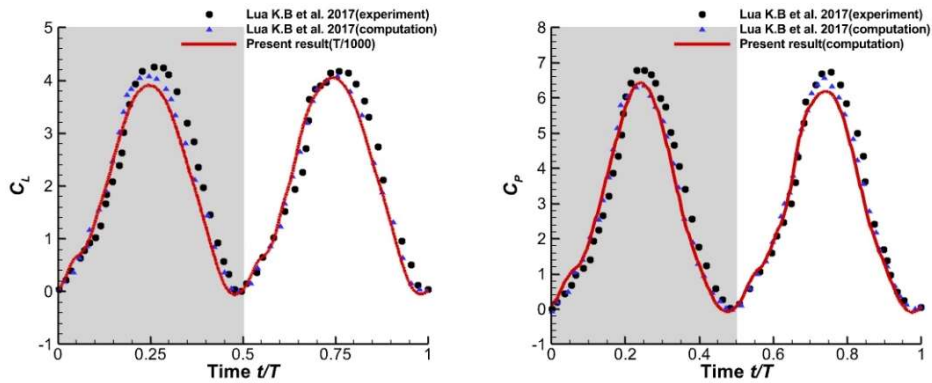

Fig. 9. Non-dimensional lift and power computed by Lua *et al.* (2017) and our simulation results. The results are taken from Figs. 5a, 5b in another paper (Lua *et al.* 2017). The present results are taken at the 5th flapping cycle when the flow becomes periodic.

force component normal to the stroke plane, the wing drag (D) as the component in the stroke plane and normal to the wingspan. In other words:

$$L = F_z, \ D = F_x \tag{7}$$

where F_z and F_x are the vertical and horizontal forces, respectively. These forces were normalized as $C_L = 2L/(\rho U^2 S)$ and $C_D = 2D/(\rho U^2 S)$. The aerodynamic power P was calculated by integrating the dot product between velocity vector and stress over the whole wing surface according to

$$P = -\int (p_n \mathbf{n} + \boldsymbol{\tau}) \mathbf{V} d|\mathbf{A}| \tag{8}$$

where p_n is static pressure, τ is wall shear stress vector, $\mathbf{V}$ is velocity vector, A is area vector, $\mathbf{n}$ is unit vector normal to the surface outward, and |A| is the magnitude of area. The power coefficient C_P was defined by normalizing the aerodynamic power P by $1/2\rho U^3$. Except for slight differences in the lift coefficient, the time courses computed for the three grids are similar, so grid 2 with 1.7 million cells is appropriate for the present study. Next, grid 2 was simulated with the time steps of $T/125$, $T/250$, and $T/500$, respectively (T = 1/f), and the simulation results were shown in Fig. 7. The time step of $T/250$ is acceptable because the inconsistencies between the results of the three cases are negligible.

2.3.4 Validation of solver

Lua *et al.* (2017) studied the lift and aerodynamic power of a three-dimensional flapping wing. We reproduced the results in a series numbered 1 where the midstroke angle of attack and the non-

dimensional time of rotation duration corresponds to 45° and 0.3, respectively. The time courses of the lift and aerodynamic power were shown in Fig. 9 for comparison. We used the same discrete schemes in time and space, boundary conditions,

grid update strategy, and solving method as those used previously. The time histories of the lift and power coefficients in the present study match well those in the previous research. There are slight differences in the force peaks due to the difference in grid update strategy. The measuring error resulted in inconsistencies between the results in the numerical simulation and the experimental measurement.

2.4 Orthogonal experiment

2.4.1 Orthogonal design

The key parameters for determining dynamic wing morphing were screen out from the model. $\Phi_{m,root}$, $\Psi_{m,tip}$, and $h_{m0,root}$ determine the degree of spanwise in-stroke-plane bending, out-of-stroke-

plane bending, and the camber in cross sections, respectively. The value of $\zeta_{m,tip}$ is larger than the value of $\zeta_{m,root}$, and the difference between the two is named the twist angle determining the degree of spanwise twist. As shown in Table 2, we picked out interesting values based on the ranges observed in hovering hummingbirds (Masateru *et al.* 2017). We first determined the maximum value of each parameter, and then changed the value slightly to make sure that it falls within the range of observations. These parameter values are explorable

Table 3 Test results from the wings in the orthogonal experiment

Series	$\Phi_{m,root}$	$\Psi_{m,tip}$	$\zeta_{m,tip}$	$h_{m0,root}$ (c_R)	Error	$\overline{C_L}$	$\overline{C_D}$	$\overline{C_P}$	η
1	47.5°	2.5°	37.5°	4%	1	0.6825	-0.0208	0.7793	0.8758
2	47.5°	5.0°	50.0°	8%	2	0.7329	-0.0323	0.8499	0.8624
3	47.5°	7.5°	62.5°	12%	3	0.7549	-0.0272	0.9630	0.7840
4	47.5°	10.0°	75.0°	16%	4	0.7509	-0.0345	1.1795	0.6366
5	50.0°	2.5°	50.0°	12%	4	0.7426	-0.0269	0.8970	0.8279
6	50.0°	5.0°	37.5°	16%	3	0.7117	-0.0324	0.9053	0.7862
7	50.0°	7.5°	75.0°	4%	2	0.6726	-0.0138	1.0134	0.6636
8	50.0°	10.0°	62.5°	8%	1	0.7486	0.0045	0.9414	0.7952
9	52.5°	2.5°	62.5°	16%	2	0.7611	-0.0131	1.0251	0.7424
10	52.5°	5.0°	75.0°	12%	1	0.7414	-0.0112	1.0922	0.6787
11	52.5°	7.5°	37.5°	8%	4	0.6982	-0.0324	0.8750	0.7980
12	52.5°	10.0°	50.0°	4%	3	0.7069	0.0023	0.8331	0.8485
13	55.0°	2.5°	75.0°	8%	3	0.7130	-0.0483	1.0290	0.6929
14	55.0°	5.0°	62.5°	4%	4	0.7362	-0.0055	0.8780	0.8384
15	55.0°	7.5°	50.0°	16%	1	0.7918	0.0059	0.9442	0.8386
16	55.0°	10.0°	37.5°	12%	2	0.7313	-0.0384	0.9286	0.7875

and valuable for the design in hummingbird-like flapping wing. We planned sixteen numerical simulations through orthogonal design. Those series were combined to making up the orthogonal experiment with four primary factors and four levels for each one in consideration. The error column was retained in Table 3 for the analysis of variance of the results. Lift is usually evaluated according to the time-averaged lift coefficient over a stroke period $\overline{C_L} = 1/T \int_0^T C_L \, dt$. And there is also correspondingly a time-averaged power coefficient $\overline{C_P} = 1/T \int_0^T C_P \, dt$. The lift efficiency, defined as the ratio of the time-averaged lift coefficient $\overline{C_L}$ to the time-averaged power coefficient $\overline{C_P}$, is thus $\eta = \overline{C_L}/\overline{C_P}$ Those are two indices to evaluate the effects of various primary factors on wing aerodynamic performance.

2.4.2 Analysis of range

The factor with a larger range has a more significant influence on the evaluation index of concern. Analysis of range is described as follows:

1. Calculate the sum K_i of the test results of the samples at the same level: $K_i = \sum_{j=1}^4 y_{i,j}$, $i = 1,2,3,4$, where i is the index of levels, j is the index of the sample, and $y_{i,j}$ is the test result of the jth sample at the ith level.
2. Calculate the average effect k_i of a factor at ith level: $k_i = K_i/4$, $i = 1,2,3,4$.
3. Calculate the range R_v : $R_v = max\{k_i\} - min\{k_i\}$, $i = 1,2,3,4$.
4. Repeat the preceding step. 1—3 to calculate and analyze the range for each factor.

2.4.3 Analysis of range (ANOVA)

Analysis of range has advantages of simplicity and intuition, but it can't distinguish the fluctuation of the results caused by the change in levels of each factor from that caused by the test error. We carried

out further analysis of variance for the test results. The ANOVA is described as follows:

1. Calculate the sum of squares (SS) of the deviations: $Y = \sum_{n=1}^{Nt} y_n/Nt$, $Nt = 16$, where n is the index of samples, y_n is the test result of the nth sample, Nt is the total number of the samples and Y is the mean of the test results of all the samples: $SS = \sum_{i=1}^4 (k_i - Y)^2$.
2. Calculate the degree of freedom (DF): $df = n - 1$, $n = 4$.
3. Calculate the mean deviation (MS): $MS = SS/df$.
4. Construct the F-statistic for each factor. $F = MS/MS_e$, where MS_e is the mean deviation under the influence of random error.
5. List the analysis of variance table to taking the statistical test.

The computed F is large enough for a factor, and then there might be more significant differences in the test result due to the different levels of the factor. Its effect on the evaluation index will be believed to be statistically significant.

3. RESULTS AND DISCUSSION

3.1 Lift and Aerodynamic Power

Sixteen simulations in Table 3 were performed. Besides, a rigid wing was supplemented to the test list for comparison. We conducted these simulations by five cycles for each series to obtain a convergent solution, and the time courses were taken at the fifth cycle when the flows became periodic. There existed a significant asymmetry in the lift force, and we attributed that to the asymmetrical kinematics of the downstroke and upstroke. However, the asymmetry observed in the lift coefficient was not so evident in the drag coefficient and power coefficient, as seen in Fig. 10b and Fig. 10c. During
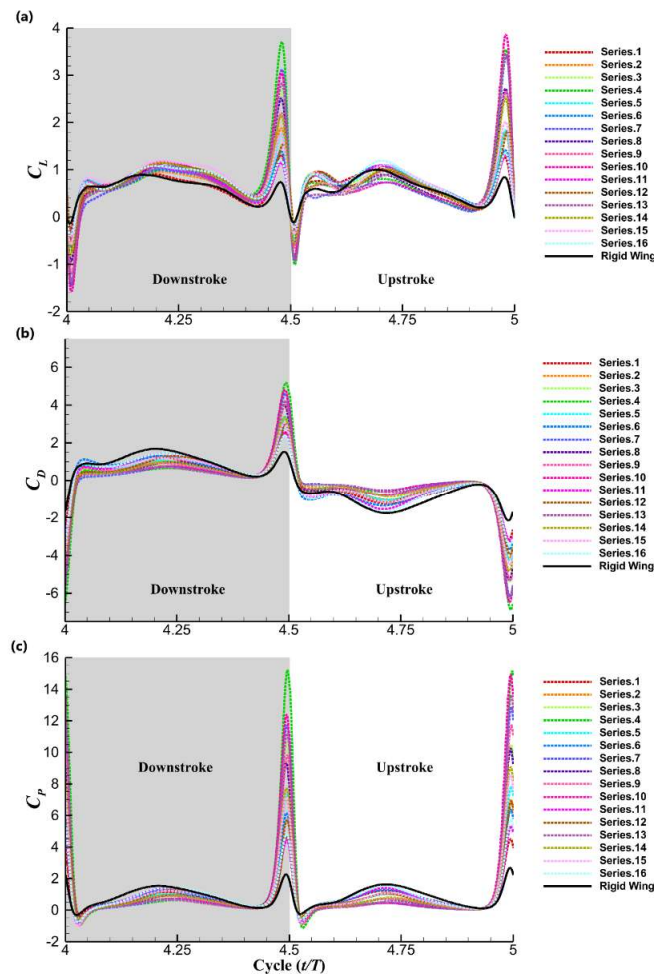
Fig. 10. Time histories of lift, drag and power coefficients of the series listed in the orthogonal experiment table during the 5th flapping cycle. A rigid wing is also added to the present experiment for comparison.

each half stroke, three local peaks occurred in the lift coefficient, corresponding to the enhancements of the wake capture, delayed stall, and rotational circulation mechanisms, respectively. A comparative result showed that the downward out-of-stroke-plane bending during the upstroke phase intensified the first two peaks in the lift coefficient by increasing the first peak and decreasing the second peak. And another noteworthy feature is that the lift coefficient generated by flexible wing declined steadily after reaching the second peak, while the high lift force was maintained for a longer duration during the downstroke phase. The first peak at the beginning of each half stroke was less affected than the third peak of lift coefficient at the end of each half stroke, which shows that the wing benefited much more from the rotational circulation. The lift coefficients display some differences in the amplitude and timing of the second peak during the translation phase, but those still vary with time in a similar way to the lift coefficient of the rigid wing.

The dynamic twist played a significant role in the generation of aerodynamic forces during the whole flapping cycle. As shown in Fig. 10a, all wings had

a negative lift generation at the beginning of each half stroke. This study has found that a decrease in the twist angle can reduce the magnitude of negative lift and increase the first peak in the lift coefficient. The wing with a moderate twist angle, such as those in series 5, 6, 15, and 16, improved the first peak. During the translation phase of the downstroke, flexible wings achieved their second lift peak later than the rigid wing and had an even higher value. The wings in series 1, 2, 5, 6, and 11 had weaker enhancement than those in series 8, 9, 10, and 14. Even though the wings in series 3, 4, 7, and 13 had large pitching angles at their tips, the enhancement was not significant during that. The main factor that changed the effect of the dynamic twist was the spanwise out-of-stroke bending of the wing because the bending and the torsion determined the effective angle of attack at each radial cross section. As the twist angle increased, the wing generated a higher peak at the end of each half stroke. The wing with a larger pitching angle at the tip had a higher rotational speed due to the constrained duration of rotation motion.

The spanwise in-stroke-plane bending harmed lift, but its influence was less significant than the

Table 4 Table about range analysis for the time-averaged lift coefficient

	$\Phi_{m,root}$	$\Psi_{m,tip}$	$\zeta_{m,tip}$	$h_{m0,root}$
K_1	2.9212	2.8992	2.8237	2.7982
K_2	2.8755	2.9222	2.9742	2.8927
K_3	2.9076	2.9175	3.0008	2.9738
K_4	2.9723	2.9377	2.8779	3.0155
k_1	0.7303	0.7248	0.7059	0.6995
k_2	0.7188	0.7305	0.7435	0.7231
k_3	0.7269	0.7293	0.7502	0.7434
k_4	0.7430	0.7344	0.7194	0.7538
R_v	0.0242	0.0096	0.0443	0.0543

Table 5 Table about range analysis for the efficiency in lift production.

	$\Phi_{m,root}$	$\Psi_{m,tip}$	$\zeta_{m,tip}$	$h_{m0,root}$
K_1	3.1588	3.1390	3.2475	3.2263
K_2	3.0729	3.1657	3.3774	3.1485
K_3	3.0676	3.0842	3.1573	3.0781
K_4	3.1574	3.0678	2.6718	3.0038
k_1	0.7897	0.7847	0.8187	0.8065
k_2	0.7682	0.7914	0.8443	0.7871
k_3	0.7669	0.7710	0.7893	0.7695
k_4	0.7893	0.7669	0.6679	0.7509
R_v	0.0228	0.0245	0.1764	0.0556

spanwise twist. The wing with a smaller elevation angle at the root produced lower lift during the downstroke phase. Furthermore, the lift force was lower during the deceleration phase. The wing with the significant spanwise bending in the stroke plane generally had lower stroke speed than the rigid wing, and the correlation between lift and bending was broken during the translation phase of the upstroke. The effect of wing twist had a more dominant role in the lift generation during this phase. As described earlier, the wing with a small pitching angle at the tip enhanced lift, while the one with a large pitching angle at the wingtip reduced lift.

Another difference between the lift coefficients of those wings exists in the timing of the second local maximum during the translation phase of the downstroke. And a long delay of the second peak was thought to be caused by the effect of the camber in cross sections. And this effect interacted with the LEVs, resulting in a longer duration of high lift during the subsequent deceleration phase. Although there were slight differences in the magnitude of the lift coefficient, a longer duration led to a larger time-averaged value. The effect of the camber in cross sections didn't seem to work during the translation phase of the upstroke.

The dynamic wing morphing reduced the power consumption throughout the flapping cycle except during the rotation phase. The aerodynamic power consumption was increased substantially in a way like that the lift was enhanced due to the large twist angle. The power coefficients had the same trends. Flexible wings had small non-dimensional power coefficients during the translation phase, especially for the wing with a large pitching angle at the tip, such as the wings in series 4,7,10, and 13. In contrast, those with a small pitching angle at the tip had large values, such as the wings in series 6, 11, and 16. During the translation and rotation phases, the wing with a moderate twist angle might consume the least power. In addition, the correlation between power consumption and twist was the most significant.

3.2 Analysis of the results in the orthogonal experiment

Table 3 lists the time-averaged lift, drag and power coefficient, and efficiency in lift production in the orthogonal experiment.

3.2.1 Analysis of the range

Range analyses for the lift coefficient and the efficiency in lift production were presented in Tables 5 and 6, respectively. According to the significance level, the four factors in Table 4 were sorted as follows: $h_{m0,root} > \zeta_{m,tip} > \Phi_{m,root} > \Psi_{m,tip}$. The analysis for the calculated average effect indicated that the lift generated by the flexible wings differed significantly due to the variations at the level of two primary factors: the camber in cross sections at the root and the pitching angle at the tip. As shown in Table 5, the effect of camber was more intuitive in that the wing with relatively more obvious camber in cross sections produced the larger time-averaged lift. The dynamic twist affected the lift generation throughout the stroke period, so it is no wonder that its effect had the second-highest significance level. A larger twist angle caused a higher positive lift peak before the stroke direction reversed and a higher negative lift peak afterward. In addition, the duration of the transition phase was so short that the lift produced during this phase didn't contribute much to the time-averaged lift. That was one of the reasons why the significance of camber effect exceeded that of wing twist effect. From the results in Table 4, the wing with a moderate pitching angle at the tip had a large time-averaged lift. This finding was consistent with the correlation between twist angle and lift coefficient observed during the translation phase. Besides, the adverse effect of the in-stroke-plane bending can be seen more clearly in Table 5 because the wing without the in-stroke-plane bending had the most time-averaged lift force generation. But it's worth noting that the wing with the most in-stroke-plane bending produced the second-highest average effect. Its value was computed according to the results from series 1, 2, 3, and 4, where the twist angle and camber were increased synchronously. Hence, the negative effect of the in-stroke-plane bending is not as effective as the combined effects of wing twist and cross-section camber. Under the dominating influence of the elevation angle at the tip, the average effect of time-averaged lift force fluctuated in relationship with the level of this factor. The spanwise out-of-stoke-plane bending was believed to be invalid. According to the results in Table 5, we determined the parameters for the deformation to maximize the lift. Their values were listed as follows: $h_{m0,root} =$

Table 6 Table about variance analysis for the time-averaged lift coefficient.

	DF	SS	MS	F
$\varphi_{m,root}$	3	0.001217	0.000406	1.34
$\Psi_{m,tip}$	3	0.000189	0.000063	0.21
$\zeta_{m,tip}$	3	0.005127	0.001709	5.65
$h_{m0,root}$	3	0.006804	0.002268	7.49
Error	3	0.000908	0.000303	——
Total	15	0.014246	——	——

Table 7 Table of variance analysis for the efficiencies

	DF	SS	MS	F
$\varphi_{m,root}$	3	0.001933	0.000654	0.85
$\Psi_{m,tip}$	3	0.001580	0.000527	0.70
$\zeta_{m,tip}$	3	0.071215	0.023738	31.40
$h_{m0,root}$	3	0.006809	0.002270	3.00
Error	3	0.002268	0.000756	——
Total	15	0.083805	——	——

$16\%c_R$, $\zeta_{m,tip} = 62.5°$, $\Phi_{m,root} = 55°$ and $\Psi_{m,tip} = 10°$ .Similarly, the four factors were ranked based on the significance level as follows: $\zeta_{m,tip} > h_{m0,root} > \Psi_{m,tip} > \Phi_{m,root}$. The spanwise twist had the most significant effect on the efficiency, while the in-stroke-plane and out-of-stroke-plane bending exhibited the same level of significance, both of which were lower than the camber effect. The increased power consumption of the highly twisted wing during the transition phase was much larger than the reduced power consumption during the translation phase, which was the reason why a large twist angle resulted in low efficiency. In addition, the wing with a moderate twist angle had the maximum average effect. The camber in cross sections decreased the efficiency, but its adverse effect was not as significant as that of the overlarge twist angle. Under the influence of either the spanwise in-stroke-plane bending or out-of-stroke-plane bending, there was subtle difference between the values of the average effect. We determined the parameters of the flexible wing with the highest efficiency, and their values were listed below: $h_{m0,root} = 4\%c_R$, $\zeta_{m,tip} = 50°$, $\Phi_{m,root} = 55°$ and $\Psi_{m,tip} = 5°$.

3.2.2 Analysis of variance

Variance analysis tables for time-averaged lift coefficient and efficiency were shown in Table 6 and 7, respectively. We arranged the factors as follows based on the magnitude of the F values in Table 6: $h_{m0,root} > \zeta_{m,tip} > \Phi_{m,root} > \Psi_{m,tip}$. It was believed that the differences in lift were primarily caused by camber and twist effect. However, they were ranked as follows according to the results in Table 7: $\zeta_{m,tip} > h_{m0,root} > \Psi_{m,tip} > \Phi_{m,root}$. The F value corresponding to the twist effect was much larger than that corresponding to any other factors. Judging from the order in the significance level, dynamic twist considerably impacted the efficiency, while other factors were not statistically significant. These conclusions were consistent with those drawn in the analysis of the range in the last section.

The optimized wings were tested and compared with the rigid wing. We presented the time courses of the lift, drag, and power coefficients in Fig. 11 and listed the time-averaged values in Table 8. The time-averaged lift coefficient of the wing with the largest time-averaged lift was 0.798 and was

increased by 35.7% compared to that of the rigid wing. But the efficiency was just increased by 10%. However, the most efficient wing produced an efficiency of 0.885, which was 25.9% higher than the efficiency of the rigid wing. The time-averaged lift coefficient of the optimized wing with the largest lift was higher than that of any other wings in the orthogonal experiment. So was the efficiency of the optimized wing with maximum efficiency. Those verified the effectiveness of orthogonal design for wing flexibility optimization.

3.3 A comparative study for the optimized wings

The net forces C_F and vector angles α_F were calculated according to

$$C_F = \sqrt{C_L{}^2 + C_D{}^2} \tag{9}$$

$$\alpha_F = tan^{-1} C_L/C_D \tag{10}$$

And the instantaneous net forces and vector angles during the fifth cycle were plotted in Fig. 12. The vector angle is a angle between the force vector and the positive x-axis, so the angle between the force vector and the horizontal stroke plane during the upstroke is$(180 - \alpha_F)°$. As the force vector tilts towards the vertical direction, the lift component outperforms the drag component, which indicates an improved aerodynamic performance. One key observation is that the instantaneous net force were reduced due to wing flexibility during the translation phase. But it caused this force to title closer to the vertical direction than in the rigid wing case. The differences in the net forces generated during the downstroke were not so significant as those generated during the upstroke. The α_F in Fig. 12 shows that the mean vector angle for the rigid wing was almost around 25°. The difference between those of the two flexible wings was slight, and they had a value close to 45°. The flexible wings with the higher mean values of α_F indicated superior aerodynamic performance than the rigid

Table 8 Time-averaged force and power coefficients, and the efficiencies in the optimized cases

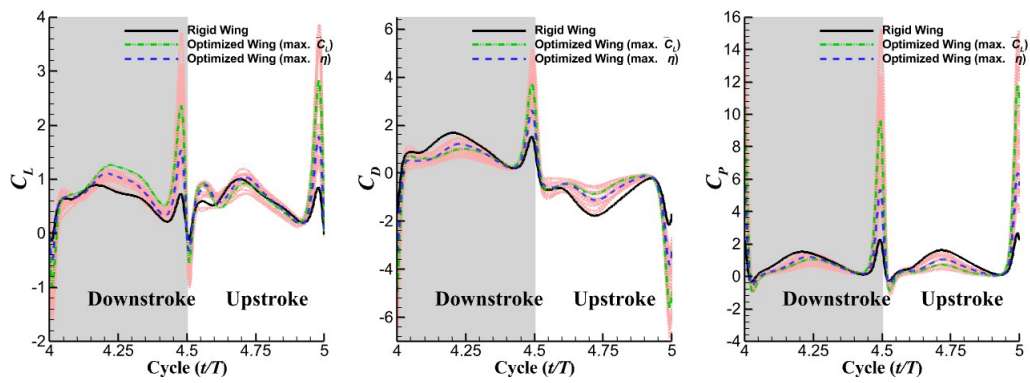| Configuration	$\overline{C_L}$	$\overline{C_D}$	$\overline{C_P}$	η
Rigid	0.588	-0.003	0.829	0.709
Max. C_L	0.798	0.009	1.023	0.780
Max. η	0.738	0.001	0.827	0.893

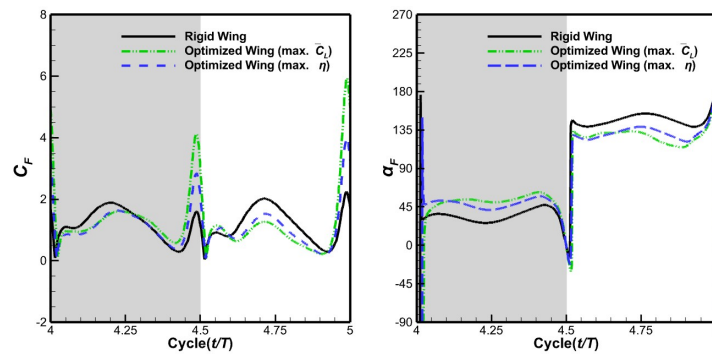**Fig. 11. Time courses of lift, drag and power coefficients of the optimized wings and the rigid wing.**

Fig. 12. Instantaneous net forces and variation of the net force angles.

(a) Optimized wing with the most lift production

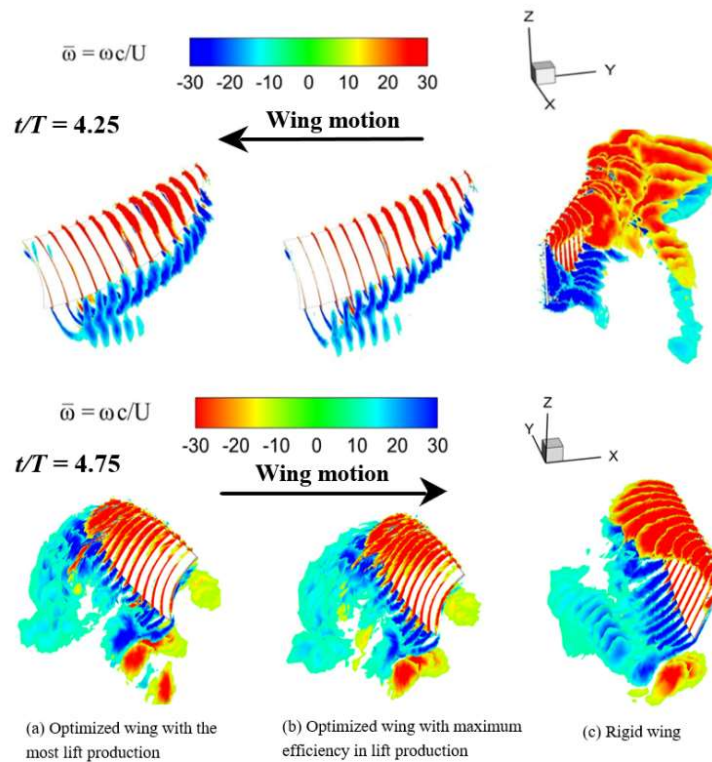(b) Optimized wing with maximum efficiency in lift production

(c) Rigid wing

Fig. 13. 3D view of vorticity distributions on the optimized flexible wings and the rigid wing at $t/T = 4.25$ and $t/T = 4.75$.

wing. However, the flexible wings produced higher peaks during the rapid rotation phase, and the enhancement was the most significant for the optimized wing with the most lift production.

In order to understand how the wing flexibility affected the vortical structures, the flow visualization was considered for $t/T = 4.25$ and $t/T = 4.75$ with the optimized wings and the rigid wing. At these time instants, the effect of wing flexibility on the peak of the generated force was more distinct in Fig. 11. The characteristics of the leading-edge and the trailing-edge vortex were investigated along the wingspan; fourteen cross sections. Normalization of the vorticities was achieved according to $\bar{\omega} = \omega c/U$. Figure 13 shows that the LEV has fully developed at these instants. At $t/T = 4.25$, one noticeable feature is that the LEV had stronger vorticity for the rigid wing but separated at the outboard section. For the optimized wings, the LEV adhered to the wall across the entire wingspan. The flexible wings stabilized the LEV near the wingtip. As shown in Fig. 12, this enhancement led to an approximately equal amount of net force generation. But the rigid wing had the most power consumption at this time instant. The leading-edge vortex and the trailing-edge vortex with opposing directions produced vorticity, and the distance between their vortex cores established a link between vorticity and the first moment of vorticity. The generated aerodynamic forces were directly proportional to the first moment of vorticity (Zhu and Sun 2017). From Fig. 13, the trailing-edge vortex was the main vortex at the inboard section since the LEVs had weaker vorticity and occupied a relatively narrower area. And the trailing-edge vortex had stronger vorticity and a further distance between the vortex cores at the inboard section, which caused the increase in the first moment of vorticity. All those have verified that the rigid wing had the most net force generation at this time instant. We concluded that the wing flexibility decreased the net force, but it also reduced power consumption. And the flexible wings produced more vertical force during the downstroke and the equivalent vertical force during the upstroke (Fig. 11). They improved the aerodynamic efficiency by using less energy to make the net force closer to the vertical direction.

4. CONCLUSION

This paper investigated several important parameters that determine the aerodynamic performance of a flexible hummingbird-inspired flapping wing in hover and their effects on the time-averaged lift force and lift efficiency. 16 series of three-dimensional numerical simulations were performed to predict the unsteady aerodynamic forces on the wing and aerodynamic power consumption. We also assessed the significance level of effect of each deformation through range analysis and variance analysis. We selected the optimum condition through the orthogonal test and statistical analysis and simulated two wings with

optimized lift and efficiency, respectively. The conclusions were summarized as follows:

- A decrease in the twist angle will reduce the magnitude of the negative lift and increase the first peak of the lift coefficient at the beginning of each stroke cycle.
- The lift coefficient produced by the highly twisted wing was relatively larger during the translation phase of the downstroke. However, that correlation disappeared during the translation phase of the upstroke.
- During the upstroke phase, the downward out-of-stroke-plane bending intensified the first two peaks of the lift coefficients by increasing the first peak and decreasing the second peak.
- Camber delayed the timing of the second lift peak. And it interacted with the LEVs to improve the magnitude of the second peak and maintained the high lift on the wing for a longer duration before the stroke changed direction.
- The in-stroke-plane bending had a weak effect on the lift production, and its positive influence only existed during the acceleration phase of the downstroke.
- the camber in cross sections was the most significant influence factor on the time-averaged lift force, while the spanwise twist had an additional impact in determining the aerodynamic efficiency during the hovering flight. The effects of the spanwise in-stroke-plane and out-of-stroke-plane bending were relatively insignificant.
- The optimized wing with the largest lift generated a time-averaged lift coefficient that was 35.7% higher than the time-averaged lift coefficient generated by the rigid wing. Besides, the efficiency produced by the optimized wing with the highest efficiency was 25.9% higher than the efficiency produced by the rigid wing. Therefore, the effect of the morphing in enhancing the wing performance was significant.
- The net force generated by the rigid wing was the largest. The wing flexibility decreased the net force, but also reduced power consumption. They improved aerodynamic efficiency by using less energy to bring the net force closer to the vertical direction.

REFERENCES

Altshuler, D. L., M. Princevac, H. Phan and J. Lozano (2009). Wake patterns of the wings and tail of hovering hummingbirds. *Experiments in Fluids* 46(5), 835-846.

Bhattacharjee, D., A. A. Paranjape and R. S. Pant (2019). Optimization of the spanwise twist of a flapping wing for bird-sized aircraft using a quasi-steady aerodynamic model. *International Journal of Aeronautical and Space Sciences* 20, 571-583.

Chin D. D and Lentink D (2016). Flapping wing aerodynamics: from insects to vertebrates. *Journal of Experimental Biology* 219(7),920-932.

Coleman, D., M. Benedict, V. Hrishikeshavan and I. Chopra (2015, May). Design, Development and Flight-Testing of a Robotic Hummingbird. *American Helicopter Society 71st Annual Forum.* Virginia Beach, Virginia.

Du, G. and M. Sun (2008). Effects of unsteady deformation of flapping wing on its aerodynamic forces. *Applied Mathematics and Mechanics* 29(6), 731-743.

Gehrke, A. (2021). Phenomenology and scaling of optimal flapping wing kinematics. *Bioinspiration & Biomimetics* 16(2), 026016-1~19.

Gehrke, A., G. Guyon-Crozier and K. Mulleners (2018). Genetic algorithm based on optimization of wing rotation in hover. *Fluids* 3(3), 59.

Keennon, M., K. Klingebiel and H. Won (2012, Jan). Development of the Nano Hummingbird: A Tailless Flapping Wing Micro Air Vehicle. In 50th AIAA Aerospace Sciences Meeting including the New Horizons Forum and Aerospace Exposition. Nashville, Tennessee.

Kim, J. K. and J. H. Han (2014). A multibody approach for 6-DOF flight dynamics and stability analysis of the hawkmoth Manduca sexta. *Bioinspiration & biomimetics* 9(1), 016011-1~21.

Lua, K. B., Y. J. Lee and T. T. Lim (2017). Water-treading motion for three-dimensional flapping wings in hover. *AIAA Journal* 55(8), 1-14.

Masateru, M., N. Toshiyuki, K. Ikuo, T. Hiroto and L. Hao (2017). Quantifying the dynamic wing morphing of hovering hummingbird. *Royal Society Open Science* 4(9), 170307-1~28.

Nan, Y., M. Karásek, M. E. Lalami and A. Preumont (2017). Experimental optimization of wing shape for a hummingbird-like flapping wing micro air vehicle. *Bioinspiration & Biomimetics* 12(2), 1-16.

Noyon, T. A., W. B. Tay, B. Oudheusden and H. Bijl (2014). Effect of chordwise deformation on unsteady aerodynamic mechanisms in hovering flapping flight. *International Journal of Micro Air Vehicles* 6(4), 265-277.

Phan, H. V., Q. T. Truong and H. C. Park (2017). An experimental comparative study of the efficiency of twisted and flat flapping wings during hovering flight. *Bioinspiration and Biomimetics* 12(3), 036009-1~13.

Phan, H. V., Q. T. Truong, T. Au and H. C. Park (2016a). Optimal flapping wing for maximum vertical aerodynamic force in hover: twisted or flat? *Bioinspiration & Biomimetics* 11(4), 046007-1~14.

Phan, H. V., T. Au and H. C. Park (2016b). Clap-and-fling mechanism in a hovering insect-like two-winged flapping-wing micro air vehicle. *Royal Society Open Science* 3(12), 160746-1~18.

Phan, H. V. and H. C. Park (2019). Insect-inspired, tailless, hover-capable flapping-wing robots: Recent progress, challenges, and future directions. *Progress in Aerospace Sciences*, 111:100573.

Reid, H., H. Zhou, M. Maxcer, R. K. Peterson and M. Jankauski (2021). Toward the design of dynamically similar artificial insect wings. *International Journal of Micro Air Vehicles* 13, 1-11.

Roccia, B. A., S. Preidikman, M. L. Verstraete and D. T. Mook (2017). Influence of Spanwise Twisting and Bending on Lift Generation in MAV-Like Flapping Wings. *Journal of Aerospace Engineering* 30(1), 04016079-1~15.

Sane, S. P. (2003). The aerodynamics of insect flight. *Journal of Experimental Biology* 206(23), 4191-4208.

Shyy, W., C-K. Kang, P. Chirarattananon, S. Ravi and H. Liu (2016). Aerodynamic, sensing and control of insect-scale flapping-wing flight. *Proceedings of The Royal Society A Mathematical Physical and Engineering Sciences* 472, 20150712-1~37.

Shyy, W., H. Aono, S. K. Chimakurthi, P. Trizila, C.-K. Kang, C. E. S. Cesnik and H. Liu (2010). Recent progress in flapping wing aerodynamics and aeroelasticity. *Progress in Aerospace Science* 46(7), 284-327.

Song, J., H. Luo and T. L. Hedrick (2014). Three-dimensional flow and lift characteristics of a hovering ruby-throated hummingbird. *Journal of the Royal Society Interface* 11(98), 20140541-1~12.

Tanaka, H., H. Suzuki, I. Kitamura, M. Maeda and H. Liu. (2013, Nov). Lift generation of hummingbird wing models with flexible loosened membranes. In *2013 IEEE/RSJ International Conference on Intelligent Robots and Systems (IROS)*, Tokyo, Japan.

Tobalske, B. W., D. R. Warrick, C. J. Clark, and D. R. Powers (2007). Three-dimensional

kinematics of hummingbird flight. *Journal of Experimental Biology* 210(13), 2368-2382.

Truong, Q. T., Q. V. Nguyen, V. T. Truong, H. C. Park and N. S. Goo (2011). A modified blade element theory for estimation of forces generated by a beetle-mimicking flapping wing system. *Bioinspiration & Biomimetics* 6(3), 036008-1~11.

Walker, S. M., A. Thomas and G. K. Taylor (2009). Deformable wing kinematics in the desert locust: how and why do camber, twist and topography vary through the stroke? *Journal of the Royal Society Interface* 6(38), 735-747.

Wolf M, Ortega-Jimenez V. M and Dudley R (2013). Structure of the vortex wake in hovering Anna's hummingbirds (Calypte anna). *Proceedings of the Royal Society B: Biological Sciences* 280(1773), 1-7.

Xuan, H., J. Hu, Y. Yu and J. Zhang (2020). Recent progress in aerodynamic modeling methods for flapping flight. *AIP Advances* 10(2), 020701-1~10.

Yang, S. and W. Zhang (2015). Numerical analysis of the three-dimensional aerodynamics of a hovering rufous hummingbird (selasphorus rufus). *Acta Mechanica Sinica* 31(6), 931-943.

Zhu, H. and M. Sun (2017). Unsteady aerodynamic force mechanisms of a hoverfly hovering with a short stroke-amplitude. *Physics of Fluids* 29(8), 081901-1~10.